

The 5–10 keV AGN luminosity function at $0.01 < z < 4.0$

S. Fotopoulou^{1,2,3,4}, J. Buchner², I. Georgantopoulos⁵, G. Hasinger^{1,6}, M. Salvato^{1,2}, A. Georgakakis^{2,5}, N. Cappelluti⁷, P. Ranalli^{5,7}, L.T. Hsu², M. Brusa^{2,7,8}, A. Comastri⁷, T. Miyaji^{9,10}, K. Nandra², J. Aird¹¹, and S. Paltani⁴

¹ Max Planck Institut für Plasma Physik, Boltzmannstrasse 2, 85748 Garching, Germany

² Max Planck Institut für Extraterrestrische Physik, Giessenbachstrasse, 85748 Garching, Germany

³ Technische Universität München, James-Franck-Strasse 1, 85748 Garching, Germany

⁴ Department of Astronomy, University of Geneva, chemin d'Ecogia 16, 1290 Versoix, Switzerland
e-mail: Sotiria.Fotopoulou@unige.ch

⁵ IAASARS, National Observatory of Athens, 15236 Penteli, Greece

⁶ Institute for Astronomy, University of Hawaii, 2680 Woodlawn Drive Honolulu, HI 96822-1839, USA

⁷ INAF-Osservatorio Astronomico di Bologna, via Ranzani 1, 40127 Bologna, Italy

⁸ Dipartimento di Fisica e Astronomia, Università di Bologna, viale Berti Pichat 6/2, 40127 Bologna, Italy

⁹ Instituto de Astronomía, Universidad Nacional Autónoma de México, Ensenada, Baja California, Mexico

¹⁰ University of California San Diego, Center for Astrophysics and Space Sciences, 9500 Gilman Drive, La Jolla, CA 92093-0424, USA

¹¹ Institute of Astronomy, University of Cambridge, Madingley Road, Cambridge CB3 0HA, UK

Received 6 August 2014 / Accepted 20 December 2015

ABSTRACT

The active galactic nuclei (AGN) X-ray luminosity function traces actively accreting supermassive black holes and is essential for the study of the properties of the AGN population, black hole evolution, and galaxy-black hole coevolution. Up to now, the AGN luminosity function has been estimated several times in soft (0.5–2 keV) and hard X-rays (2–10 keV). AGN selection in these energy ranges often suffers from identification and redshift incompleteness and, at the same time, photoelectric absorption can obscure a significant amount of the X-ray radiation. We estimate the evolution of the luminosity function in the 5–10 keV band, where we effectively avoid the absorbed part of the spectrum, rendering absorption corrections unnecessary up to $N_{\text{H}} \sim 10^{23} \text{ cm}^{-2}$. Our dataset is a compilation of six wide, and deep fields: MAXI, HBSS, XMM-COSMOS, Lockman Hole, XMM-CDFS, AEGIS-XD, *Chandra*-COSMOS, and *Chandra*-CDFS. This extensive sample of ~ 1110 AGN ($0.01 < z < 4.0$, $41 < \log L_x < 46$) is 98% redshift complete with 68% spectroscopic redshifts. For sources lacking a spectroscopic redshift estimation we use the probability distribution function of photometric redshift estimation specifically tuned for AGN, and a flat probability distribution function for sources with no redshift information. We use Bayesian analysis to select the best parametric model from simple pure luminosity and pure density evolution to more complicated luminosity and density evolution and luminosity-dependent density evolution (LDDE). We estimate the model parameters that describe best our dataset separately for each survey and for the combined sample. We show that, according to Bayesian model selection, the preferred model for our dataset is the LDDE. Our estimation of the AGN luminosity function does not require any assumption on the AGN absorption and is in good agreement with previous works in the 2–10 keV energy band based on X-ray hardness ratios to model the absorption in AGN up to redshift three. Our sample does not show evidence of a rapid decline of the AGN luminosity function up to redshift four.

Key words. galaxies: active – quasars: supermassive black holes

1. Introduction

The X-ray luminosity function (XLF) of active galactic nuclei (AGN) and its evolution provides a view of black hole (BH) growth across cosmic time. Several studies use the XLF to constrain models of BH evolution through simulations and semi-analytic models (e.g., Mahmood et al. 2005; Hopkins et al. 2005a; Hirschmann et al. 2012, 2014; Enoki et al. 2014) and to investigate the possible galaxy-BH coevolution (e.g., Hopkins et al. 2007; Marulli et al. 2008; Zheng et al. 2009; Fanidakis et al. 2011). The XLF is also used to constrain the properties of the AGN population, for example, by creating population synthesis models that describe the cosmic X-ray background (CXB) and thus inferring the fraction of Compton-thick AGN (e.g., Gilli et al. 2007; Treister et al. 2009; Draper & Ballantyne 2009; Akylas et al. 2012). Additionally, the XLF is used to test the still

open question of AGN triggering: mergers vs secular processes (Draper & Ballantyne 2012). The multivariate changes of the AGN phase can be studied by combining the XLF with luminosity functions in other wavelengths (e.g., Han et al. 2012; Hopkins et al. 2005b). For example, the connection between X-ray and infrared radiation from AGN has been studied by means of reconciling the CXB with the infrared background through the corresponding luminosity functions (Ballantyne & Papovich 2007).

Early X-ray surveys showed that the space density of AGN follows a broken power-law distribution and it was proposed that the XLF only evolves with redshift in luminosity (pure luminosity evolution, hereafter PLE; Maccacaro et al. 1983, 1984), while subsequent studies showed that the evolution stops, or dramatically slows down after a critical redshift value (e.g. Boyle et al. 1994; Page et al. 1996; Jones et al. 1997). Recent works in the soft X-ray regime (0.5–2 keV) support a

luminosity-dependent density evolution (LDDE) over the simple PLE with the number density of AGN peaking in redshift $z = 1-2$ (Miyaji et al. 2000; Hasinger et al. 2005; Ebrero et al. 2009). Similarly in the hard X-ray band (2–10 keV) several works support LDDE over PLE (Ueda et al. 2003; La Franca et al. 2005; Ebrero et al. 2009; Ueda et al. 2014; Miyaji et al. 2015). Other studies at the same energy band also tested simultaneous variations in luminosity and density with different parametrization, namely, independent luminosity and density evolution (ILDE; Yencho et al. 2009) and luminosity and density evolution (LADE; Aird et al. 2010).

According to the unified model of AGN (Antonucci 1993; Urry & Padovani 1995), a supermassive black hole is found at the center of each AGN, surrounded by an accretion disk and a torus of gas and dust. The current accepted view of the radiation mechanism includes X-ray production in the vicinity of the black hole through Comptonization of disk photons in a population of hot thermal electrons (Haardt & Maraschi 1993). The torus is responsible for the obscuration of X-rays due to photoelectric absorption. The torus also generates infrared emission, which is optical radiation reprocessed by the dust. For the luminosity function in the X-ray energy ranges 0.5–2 keV and 2–10 keV, a correction factor must be applied depending on the absorption power of the obscuring torus in each source. This absorption power is either calculated from the spectrum or roughly estimated from the observed flux in at least two X-ray energy bands. An additional correction factor is often applied to take redshift incompleteness into account in the sample under investigation.

In this work, we study X-ray emission in a hard band (5–10 keV), avoiding the absorbed part of the spectrum. Previous works over the same energy range attempted to put constraints on the bright end of the 5–10 keV XLF. La Franca et al. (2002) used ~ 160 AGN detected in BeppoSAX, ASCA, and HEAO 1 with a flux limit of $F_x = 3 \times 10^{-14}$ erg s $^{-1}$ cm $^{-2}$, while Ebrero et al. (2009) used a sample of ~ 120 XMM detected AGN with a flux limit of $F_x = 6.8 \times 10^{-15}$ erg s $^{-1}$ cm $^{-2}$. The small number of available AGN was not enough to differentiate between PLE and LDDE models and the authors resorted to fixing the evolutionary parameters of the luminosity function. Similarly, efforts have been made to determine the X-ray luminosity function at energies higher than 10 keV using objects detected with INTEGRAL and *Swift*-BAT (Beckmann et al. 2006; Sazonov et al. 2007; Paltani et al. 2008; Burlon et al. 2011). These samples include very bright local objects ($z < 0.1$), which put constraints on the local luminosity function, but are not able to constrain the evolution of the AGN number density with redshift.

With the combination of recent multiwavelength surveys, we are able to create a sizable sample of ~ 1100 sources with a flux limit of about $F_x = 1.5 \times 10^{-16}$ erg s $^{-1}$ cm $^{-2}$, which is 10 times deeper and 5–6 times more numerous than previously available samples in the same energy range. Spectroscopic redshifts (spec- z), combined with accurate photometric redshifts (photo- z), provide a 98% redshift complete sample that is ideal for probing AGN evolution. We determine the XLF and its evolution in the 5–10 keV band testing the evolutionary models used in the literature. We perform Bayesian analysis to investigate in detail the probability distribution function for each parameter that describes the luminosity function, per survey and in the combined sample. This approach provides an accurate view of the parameters without assuming Gaussian distribution around the best value. In Sect. 2.1 we present the surveys used for this work, and in Sect. 2.2 we discuss the selection of the 5–10 keV energy range. In Sect. 3 we describe the models we used in

estimating the luminosity function. In Sect. 4 we describe our analysis and the selection of the best model for our dataset. In Sect. 5 we discuss the LDDE model, compare the information contained in each survey separately, and predict the expected number of AGN for future surveys. We adopt the cosmological parameters $\Omega_\Lambda = 0.7$, $\Omega_m = 0.3$, and $H_0 = 70$ km s $^{-1}$ Mpc $^{-1}$.

2. Dataset definition

We combined wide/medium angle surveys (MAXI, HBSS, COSMOS) with pencil beam X-ray fields (Lockman Hole (LH), AEGIS, CDFS) to create a sample of 5–10 keV detected AGN. We exclude known stars, galaxies, and galaxy clusters from these samples. The combined sample consists of 1115 AGN with luminosities between 10^{41} – 10^{47} erg s $^{-1}$ in the redshift range $0.01 < z < 5$. As can be seen from Fig. 1a, about ten sources have luminosity between $41 < \log L < 42$; this amounts to roughly 1% of our sample. We have tested that using a limit of 10^{42} erg s $^{-1}$ or 10^{41} erg s $^{-1}$ does not significantly alter the estimation of the luminosity function parameters. Good coverage of the luminosity – redshift plane (Fig. 1a) was possible as a result of the wide range of sky coverage and X-ray depth reached with the combination of these fields (Fig. 1b).

The sample is 98% complete in redshift, and 68% of the redshifts is spectroscopically determined. The remaining 29.7% of the sample consists of sources from the fields XMM-COSMOS, Lockman Hole, AEGIS, and *Chandra* Deep Field South, where the multiwavelength coverage of the fields facilitated the computation of accurate photometric redshifts. The accuracy in all fields is better than $\sigma_{\text{NMAD}} = 0.07$ with a small fraction of outliers (Salvato et al. 2009, 2011; Fotopoulou et al. 2012; Hsu et al. 2014; Nandra et al. 2015; Aird et al. 2015). All photometric redshifts were obtained with the SED fitting code LePhare¹, and we use the redshift probability distribution function for our analysis. The probability distribution function is proportional to $e^{-\chi_{\text{min}}^2(z)/2}$, where χ_{min}^2 refers to the galaxy or AGN template with the minimum χ^2 at a given redshift. This function is normalized to 1 to obtain the probability distribution function. We assign a flat probability distribution function in the range $z = 0-7$ for sources for which no photometric redshift determination is possible.

2.1. Surveys

MAXI extragalactic survey. The Monitor of All-sky X-ray Image (MAXI) mission on board the International Space Station (ISS) observes the entire sky every 92 min with two instantaneous fields of view covering each $160^\circ \times 3^\circ$. MAXI consists of two cameras, the Gas Slit Camera (GSC; Sugizaki et al. 2011; Mihara et al. 2011) sensitive in the 2–30 keV energy band and the Solid-state Slit Camera (SSC; Tsunemi et al. 2010; Tomida et al. 2011) sensitive in the 0.5–12 keV energy band. Hiroi et al. (2011) presented the first MAXI/GSC seven-month data catalog of sources detected in the 4–10 keV band and at high Galactic latitudes ($|b| > 10^\circ$, 34 000 deg 2). Ueda et al. (2011) used 37 AGN from this catalog to compute the local AGN luminosity function. Here we are using the 22 AGN out of the 37 AGN presented in Ueda et al. (2011) that have spectroscopic redshift $z > 0.01$. The flux limit² of the sample

¹ <http://www.cfht.hawaii.edu/~arnouts/LEPHARE/lephare.html>

² As a flux limit, we quote the flux of the faintest source in the sample.

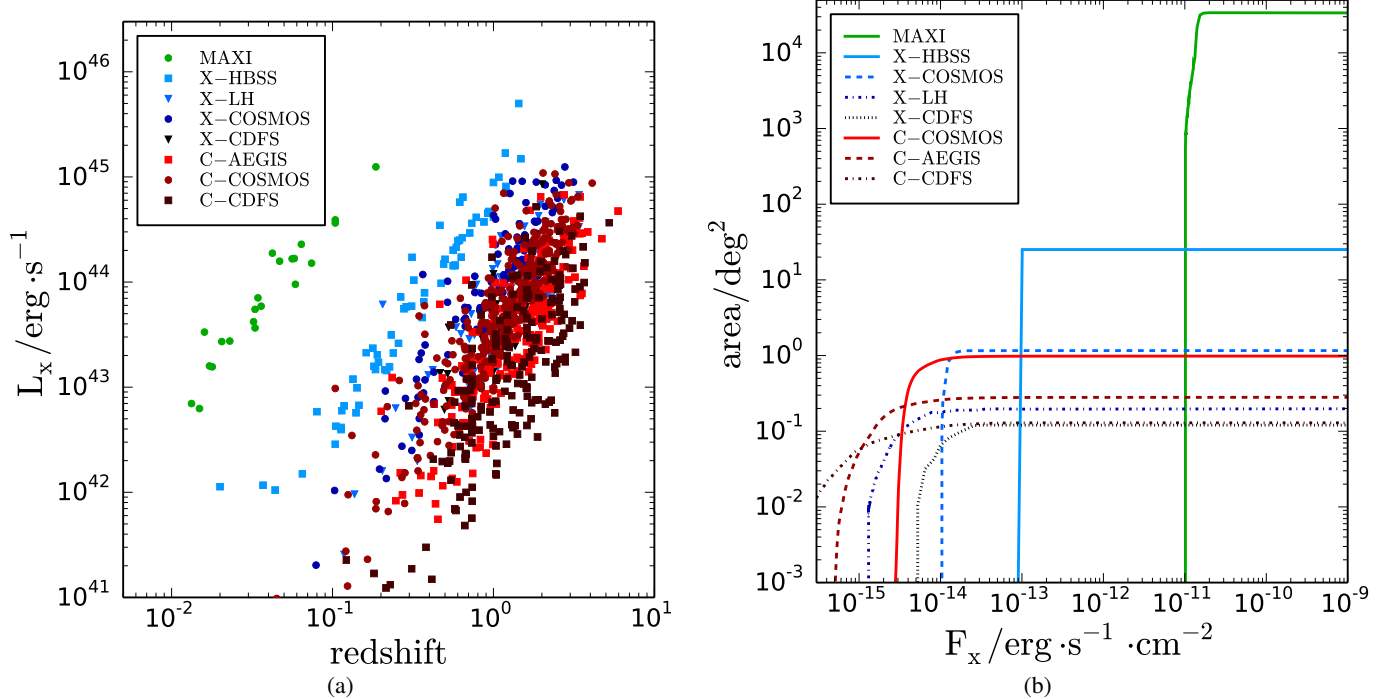


Fig. 1. a) 5–10 keV luminosity – redshift plane, showing sources with either spectroscopic or photometric redshift estimation. b) Sky coverage as a function of X-ray flux for each survey.

is $F_x = 1.1 \times 10^{-11} \text{ erg s}^{-1} \text{ cm}^{-2}$ covering a redshift range $0.01 < z < 0.19$ with median redshift $z = 0.034$ and median luminosity $\log L_x = 43.85$.

Hard Bright Serendipitous Survey (HBSS). The *XMM-Newton* Bright Serendipitous Survey covers 25 deg^2 (Della Ceca et al. 2004) and provides two flux limited samples in the 0.5–4.5 keV and 4.5–7.5 keV band. We are using the hard sample 4.5–7.5 keV with a flux limit of $F_x = 1 \times 10^{-13} \text{ erg s}^{-1} \text{ cm}^{-2}$. The optical counterparts and spectroscopic redshifts are presented in Caccianiga et al. (2008). The sources cover the redshift range $0.02 < z < 1.48$ with median redshift $z = 0.312$ and median luminosity $\log L_x = 43.8$. This survey covers a large area introducing sample rare bright objects at higher redshift compared to MAXI.

XMM-COSMOS. The XMM-COSMOS field is one of the widest contiguous XMM fields covering 2 deg^2 . The XMM-COSMOS field contains 245 sources detected in the 5–10 keV (Cappelluti et al. 2009), with a flux limit of $F_x = 5 \times 10^{-15} \text{ erg s}^{-1} \text{ cm}^{-2}$ and a good balance between depth and sky coverage. The unprecedented multiwavelength coverage of this field provides optical (Capak et al. 2007), ultraviolet (Zamojski et al. 2007), near-infrared (McCracken et al. 2010), mid-infrared (Sanders et al. 2007; Ilbert et al. 2009; Frayer et al. 2009) counterparts, and spectroscopic redshifts (Trump et al. 2009; Lilly et al. 2007, 2009) (see Brusa et al. 2007, 2010, for a summary). For 79.2% of the sample spectroscopic redshifts are available, while the remaining 18.3% of the sample has high quality photometric redshifts (Salvato et al. 2009, 2011) reaching a total of 97.5% redshift completeness. The X-COSMOS sources span a redshift range $0.04 < z < 3.14$, with a median redshift of $z = 1.1$ and median luminosity $\log L_x = 44.05$.

XMM – Lockman Hole (LH). The Lockman Hole is one of the deepest *XMM-Newton* fields. The X-ray catalog presented in Brunner et al. (2008) contains 88 sources detected in the 5–10 keV band and the optical counterparts are presented in Rovilos et al. (2011) with flux limit $F_x = 2 \times 10^{-15} \text{ erg s}^{-1} \text{ cm}^{-2}$. Photometric redshifts are presented in Fotopoulou et al. (2012) reaching 98.8% completeness. The Lockman Hole dataset provides faint sources detected with XMM, allowing us to probe the faint end of the luminosity function at redshift above 0.5. This dataset covers a redshift range of $0.118 < z < 3.41$ with median redshift $z = 1.192$ and median luminosity $\log L_x = 43.78$.

XMM – Chandra Deep Field South (XMM – CDFS). The CDFS has been observed by XMM for a total exposure of 3.5 Ms. We include the 5–10 keV detections presented in Ranalli et al. (2013), where the optical identification and spectroscopic redshift sample is also described. The XMM observations reach a flux limit of $F_x = 8 \times 10^{-16} \text{ erg s}^{-1} \text{ cm}^{-2}$. The photometric redshift described in Hsu et al. (2014) are specifically tuned for AGN and show improved accuracy over previous estimations for the same area. This dataset covers a redshift range of $0.5 < z < 2.5$ with median redshift $z = 1.22$ and median luminosity $\log L_x = 43.58$.

Chandra-COSMOS. The COSMOS field has also been observed with the *Chandra* observatory, and we use the 160 ks C-COSMOS observations of Elvis et al. (2009) covering an area of $\sim 1.0 \text{ deg}^2$. The reduction of the X-ray data is performed as described in Laird et al. (2009), yielding 357 sources detected in the 4–7 keV energy band with flux limit $F_x = 1.8 \times 10^{-15} \text{ erg s}^{-1} \text{ cm}^{-2}$. The counterpart association and photo- z estimation are described in Aird et al. (2015). The *Chandra-COSMOS* sources span a redshift range $0.04 < z < 4.1$ with a median redshift of $z = 1.2$ and median luminosity $\log L_x = 43.75$.

Table 1. Redshift information per X-ray field.

Field	Area (deg ²)	No. sources	Spec-z	Photo-z	No redshift	Median redshift	Completeness	Redshift range
MAXI	33 800	22	22	0	0	0.04	100%	0.01–0.19
XMM-HBSS	25	64	62	0	2	0.31	96.9%	0.02–1.48
XMM-COSMOS ^a	2.15/1.16	245/115	194/83	45/30	6/2	1.07/1.06	97.5%/98.3%	0.04–3.14
XMM-LH	0.2	88	50	38	0	1.19	100%	0.12–3.41
XMM-CDFS ^a	0.26/0.12	137/30	109/18	24/8	4/4	1.31/1.22	97.1%/86.7%	0.12–3.8
<i>Chandra</i> -COSMOS	0.98	357	257	87	13	1.21	96.4%	0.04–4.1
<i>Chandra</i> -AEGIS-XD	0.28	244	133	111	0	1.51	100%	0.04–5.9
<i>Chandra</i> -CDFS	0.13	195	136	58	1	1.36	99.5%	0.1–5.2
Total sample ^b	33828	1115	761	332	22	1.19	98%	0.01–5.9

Notes. ^(a) Numbers refer to the full XMM field/not overlapping with *Chandra* area, respectively. ^(b) Removing the overlapping area of XMM and *Chandra* observations in the COSMOS and CDFS fields as described in the text.

AEGIS-XD. The AEGIS-XD field spans an area of 0.2 deg² and benefits from multiwavelength coverage. The X-ray detection was performed with *Chandra* in the 4–7 keV energy range, and the counts were transformed to flux in the 5–10 keV range, assuming that the X-ray spectrum is a power-law with $\Gamma = 1.4$ (Nandra et al. 2015). The optical counterparts were retrieved with a likelihood ratio approach, using the Rainbow Cosmological Surveys Database (Barro et al. 2011a,b). Spectroscopic redshifts are a compilation from the DEEP2 (Newman et al. 2012) and DEEP3 fields (Cooper et al. 2012) and from the MMT (Coil et al. 2009). The AEGIS-XD survey is one of the two surveys with large number of objects in our sample with twice the area of LH and XMM-CDFS. The flux limit of AEGIS-XD is $F_x = 5.9 \times 10^{-16}$ erg s⁻¹ cm⁻² and the sources cover the redshift range $0.05 < z < 3.85$ with median redshift $z = 1.53$ and median luminosity $\log L_x = 43.64$.

Chandra – Chandra Deep Field South (Chandra – CDFS). The CDFS is the deepest to date X-ray field, covering an area of 0.1 deg². We use the 4 Ms observations (Xue et al. 2011), reduced as described in Laird et al. (2009), similar to the *Chandra*-COSMOS observations. The counterpart assignment is described in Aird et al. (2015), while the photo- z estimation are the same as for XMM-CDFS presented in Hsu et al. (2014). The flux limit of *Chandra* – CDFS is $F_x = 1.4 \times 10^{-16}$ erg s⁻¹ cm⁻². The *Chandra*-CDFS contains 195 sources spanning a redshift range $0.1 < z < 5.2$ with a median redshift of $z = 1.3$ and median luminosity $\log L_x = 43.2$.

Avni & Bahcall (1980) introduced the coherent volume addition to analyze independent samples simultaneously. The main idea is that a source is considered detectable in any of the surveys as long as it is above the detection threshold for that particular survey. From the samples gathered for this work, sources in COSMOS and CDFS appear twice when considering both the XMM and *Chandra* observations since the fields partially overlap on the sky. Miyaji et al. (2015) solved this issue by merging the detection lists and creating an effective area curve that describes both XMM and *Chandra* COSMOS observations. Here instead we adopt a different strategy. Since both *Chandra*-COSMOS and *Chandra*-CDFS cover a smaller area than the respective XMM observations, we keep the entire *Chandra* field and select the XMM observations that do not fall in the *Chandra* area. With this approach, we have two independent fields profiting both from the depth of the *Chandra* observations and the

wider area covered by XMM. In Table 1 we gather the area coverage, number of detected sources, and redshift information for all fields.

2.2. 5–10 keV selection

AGN X-ray spectra above 1 keV can be described adequately as a power-law distribution, $F(E) \propto E^{-\Gamma}$, with $\Gamma = 1.4$ –1.6 for radio loud AGN and $\Gamma = 1.8$ –2.0 for radio-quiet AGN (Nandra & Pounds 1994; Reeves & Turner 2000; Piconcelli et al. 2005; Page et al. 2005; Mateos et al. 2005). We calculate theoretical flux and count rate values for different N_H and redshift values, assuming a power-law spectrum with photon index $\Gamma = 1.9$ via models *zphabs*cuttoffpl* in PyXspec, the Python interface to Xspec (Arnaud 1996). In Fig. 2 we plot the expected flux ratio for three N_H values as a function of redshift. The blue lines correspond to the 5–10 keV energy band and the red lines correspond to the 2–10 keV energy band. We show that even for high absorbing column densities such as 10^{23} cm⁻², the observed flux in the 5–10 keV energy range is more than 90% of the intrinsic for $z > 1$, and never less than 80% even at lower redshifts. In this plot we do not include the effect of Thompson scattering, which would reduce the flux up to 2.3% and 18.8% in the 2–10 keV band at $\log N_H = 22$ and $\log N_H = 23$, respectively.

XMM-Newton and *Chandra* are less sensitive to energies above 7 keV. Therefore, only bright sources are detected in the 5–10 keV energy band since typically the detection limit in this band is an order of magnitude higher compared to the 0.5–2 keV energy band. Consequently, this work does not include very faint sources ($F_x < 5.9 \times 10^{-16}$ erg s⁻¹ cm⁻²). Even though there are interesting cases on an individual source basis, we do not expect differences in a study of the global population as it has been demonstrated that the 5–10 keV does not select a special AGN population (Della Ceca et al. 2008).

3. Modeling the luminosity function

Early observations of X-ray AGN showed that the local luminosity function ($z \sim 0$) is well described by a broken power-law distribution (Maccacaro et al. 1983, 1984)

$$\frac{d\phi(L, z = 0)}{d \log L} = \frac{A}{\left(\frac{L}{L_0}\right)^{\gamma_1} + \left(\frac{L}{L_0}\right)^{\gamma_2}}, \quad (1)$$

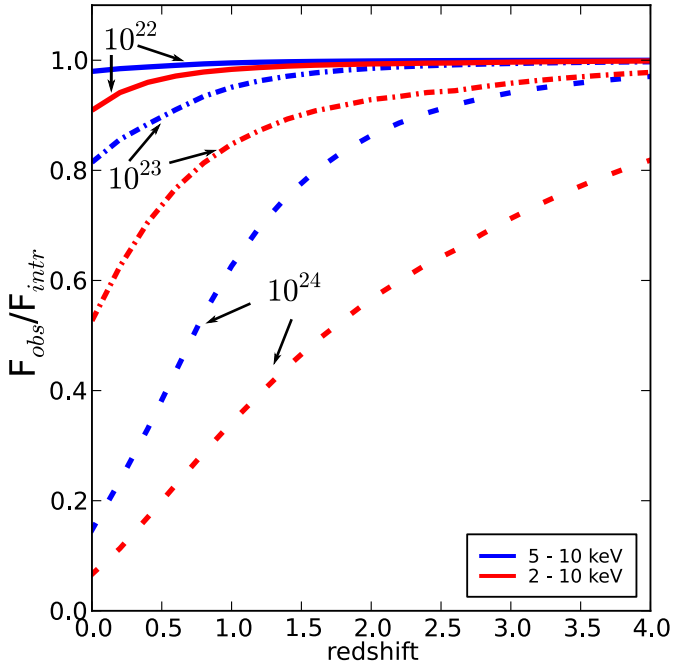


Fig. 2. Observed flux over intrinsic flux for a power-law spectrum with photoelectric absorption in the 5–10 keV band (blue) and 2–10 keV energy band (red). The observed 5–10 keV flux is never lower than 80% of the intrinsic at all redshifts and for column densities up to $\log N_{\text{H}} = 23$.

where L_0 , is the luminosity at which the break occurs and γ_1 , γ_2 are the slopes of the power-law distributions below and above L_0 .

Several works thereafter have concluded that the luminosity function shows a strong evolution with redshift (e.g., Boyle et al. 1994; Page et al. 1996; Jones et al. 1997). We test the most commonly used models to describe the evolution of the luminosity function. In the rest of this section we give the formula and a brief physical description of each model. In Fig. 3 we show a qualitative overview of the differential luminosity function versus the luminosity computed at several redshifts given by the color scale. In these plots the critical redshift after which the evolution changes has been set to $z_c = 1.8$ when applicable.

3.1. Pure luminosity evolution

The first modification of the broken power-law model to include evolution, PLE, was examined by Schmidt (1968). The evolution is most commonly expressed as (Miyaji et al. 2000; Ueda et al. 2003; La Franca et al. 2005; Ebrero et al. 2009)

$$\frac{d\phi(L, z)}{d \log L} = \frac{d\phi(L/e(z), z = 0)}{d \log L} \quad (2)$$

with,

$$e(z) = \begin{cases} (1+z)^{p_1} & z \leq z_c \\ (1+z_c)^{p_1} \cdot \left(\frac{1+z}{1+z_c}\right)^{p_2} & z \geq z_c, \end{cases} \quad (3)$$

where z_c the redshift after which the evolution, $e(z)$, changes behavior and also follows a broken power law with slopes dependent on p_1 and p_2 . As seen from Fig. 3, the PLE model is apparent as a shift of the luminosity function from higher to lower luminosities when moving from higher to lower redshift.

Since the shape of the luminosity function is assumed to remain the same, this would be interpreted as a change in luminosity of the global AGN population.

3.2. Pure density evolution

The PDE model was also examined in the very early studies of luminosity function evolution (Schmidt 1968) and it is usually expressed as

$$\frac{d\phi(L, z)}{d \log L} = \frac{d\phi(L, z = 0)}{d \log L} \cdot e(z), \quad (4)$$

with the evolutionary factor, $e(z)$, given by Eq. (3). The physical interpretation of this model is that AGN change in numbers, but their luminosities remain constant. This would be possible if the transition from active to inactive phase and vice versa were rapid and thus hardly observable. This evolution would appear as a change in the normalization of the luminosity function (see Fig. 3).

3.3. Independent luminosity density evolution

The ILDE model was used by Yenko et al. (2009) to describe the evolution of AGN for redshifts below $z = 1.2$. This model postulates that there is a simultaneous change in luminosity and number of AGN. Since this model is confined below redshift $z < 1.2$, no critical redshift value was introduced, i.e.,

$$\frac{d\phi(L, z)}{d \log L} = \frac{d\phi(L/e_L(z), z = 0)}{d \log L} e_D(z) \quad (5)$$

with,

$$e_L(z) = (1+z)^{p_L} \quad (6)$$

and

$$e_D(z) = (1+z)^{p_D}, \quad (7)$$

similar to the PLE (Eq. (3)) and PDE (Eq. (4)) models below z_c .

3.4. Luminosity and density evolution

The LADE model was introduced by Aird et al. (2010). This model enables independent evolution of the luminosity function both in luminosity and number density, but with the inclusion of a critical redshift value,

$$\frac{d\phi(L, z)}{d \log L} = \frac{d\phi(L/e_L(z), z = 0)}{d \log L} \cdot e_d(z). \quad (8)$$

The luminosity evolution follows a broken power law

$$e_L(z) = \left(\frac{1+z_c}{1+z}\right)^{p_1} + \left(\frac{1+z_c}{1+z}\right)^{p_2}, \quad (9)$$

while the evolution in number density follows a power law given by

$$e_d(z) = 10^{d(1+z)}. \quad (10)$$

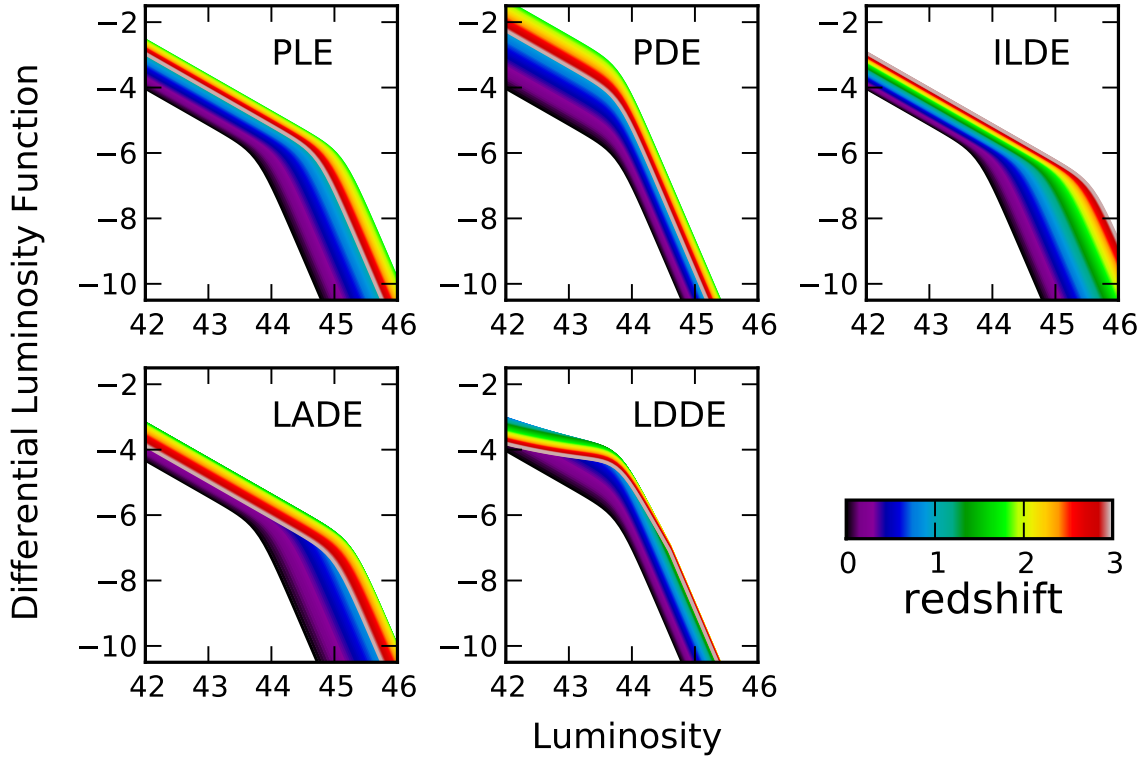


Fig. 3. Comparison of common AGN luminosity function evolutionary models. Models computed with fictitious evolutionary parameters to demonstrate the qualitative difference in evolution. The color scale shows the evolution of each model with redshift ranging from $z = 0$ (black) to $z = 3$ (red). The critical redshift is chosen $z_c = 1.8$ (bright green) for all models.

3.5. Luminosity-dependent density evolution

The LDDE model was introduced by [Schmidt & Green \(1983\)](#) to describe the evolution of optically selected quasars. [Miyaji et al. \(2000\)](#) introduced a formalism to describe the soft X-ray luminosity function of type 1 (unabsorbed) AGN, which has been extensively used ever since. This more complex model encapsulates the fact that the number density of AGN changes, but since the evolution of bright and low-luminosity AGN exhibits different timescales, the critical redshift, z_c , depends on the luminosity.

We use the formalism introduced by [Ueda et al. \(2003\)](#) as follows:

$$\frac{d\phi(L, z)}{d \log L} = \frac{d\phi(L, z=0)}{d \log L} \cdot e(L, z) \quad (11)$$

with,

$$e(L, z) = \begin{cases} (1+z)^{p_1} & z \leq z_c(L) \\ (1+z_c)^{p_1} \cdot \left(\frac{1+z}{1+z_c}\right)^{p_2} & z \geq z_c(L) \end{cases} \quad (12)$$

and

$$z_c(L) = \begin{cases} z_c^* & L \geq L_a \\ z_c^* \cdot \left(\frac{L}{L_a}\right)^a & L < L_a. \end{cases} \quad (13)$$

We express the evolution factor $e(L, z)$ of Eq. (12) as

$$e(z, L) = \frac{(1+z_c)^{p_1} + (1+z_c)^{p_2}}{\left(\frac{1+z}{1+z_c}\right)^{-p_1} + \left(\frac{1+z}{1+z_c}\right)^{-p_2}}, \quad (14)$$

with z_c defined as in Eq. (13). This formula is equivalent to the [Ueda et al. \(2003\)](#) evolution factor, creating a smooth transition of the XLF before and after the critical redshift, and it is normalized correctly at redshift zero.

[Ueda et al. \(2014\)](#), motivated by the results obtained by the COSMOS team at high redshift, (XMM-COSMOS; [Brusa et al. 2009](#); *Chandra*-COSMOS; [Civano et al. 2011](#)) introduced a more complicated model to describe the drop in number density above $z \sim 3$. In their formalism, an additional cutoff redshift is used, while the evolution index p_1 is luminosity dependent as introduced by [Miyaji et al. \(2000\)](#). In [Ueda et al. \(2014\)](#), the evolutionary factor $e(L, z)$ is given by

$$e(L, z) = \begin{cases} (1+z)^{p_1} & z \leq z_{c1}(L) \\ (1+z_{c1})^{p_1} \cdot \left(\frac{1+z}{1+z_{c1}}\right)^{p_2} & z_{c1}(L) < z \leq z_{c2}(L) \\ (1+z_{c1})^{p_1} \cdot \left(\frac{1+z_{c2}}{1+z_{c1}}\right)^{p_2} \cdot \left(\frac{1+z}{1+z_{c2}}\right)^{p_3} & z \geq z_{c2}(L), \end{cases} \quad (15)$$

where

$$z_{c1,2}(L) = \begin{cases} z_{c1,2}^* & L \geq L_{a1,2} \\ z_{c1,2}^* \cdot \left(\frac{L}{L_{a1,2}}\right)^a & L < L_{a1,2} \end{cases} \quad (16)$$

and

$$p_1(L) = p_1^* + \beta_1(\log L - \log L_p). \quad (17)$$

We refer to this expression of LDDE hereafter as Ueda14.

4. The 5–10 keV luminosity function

In this section, we present our procedure for the parameter estimation for the aforementioned models. We identify the model

that best describes our dataset based on the Akaike information criterion (AIC) and Bayesian information criterion (BIC).

4.1. Model parameter estimation

According to the Bayes theorem, the posterior probability of the model parameters θ , given the observed data D and the model M , $p(\theta|D, M)$, is proportional to the probability of prior knowledge of the model parameters θ , $p(\theta|M)$, times the likelihood of observing the collected data D , under the given model M and set of model parameters θ , $p(D|\theta, M)$ as follows:

$$p(\theta|D, M) = \frac{p(\theta|M)p(D|\theta, M)}{\int p(\theta|M)p(D|\theta, M)d\theta} \quad (18)$$

Treating the observation of n sources out of the available N AGN in the Universe as a Poisson process³ (applicable in the limit $n/N \ll 1$) (Marshall et al. 1983), the likelihood⁴ of observing n sources is given by

$$\begin{aligned} \ln \mathcal{L}(L, z) = & \sum_{i=1}^n \ln \int \int \phi(z_i, \log L_{xi}) p_i(\log L, z) \frac{dV_c}{dz} dz d \log L \\ & - \int \int \phi(z, \log L) \Omega(z, \log L) \frac{dV_c}{dz} dz d \log L, \end{aligned} \quad (19)$$

where $\phi(z, \log L)$ is the model of the luminosity function, $p(\log L, z)$ the uncertainties on the luminosity and redshift for each observed source, dV_c/dz the differential comoving volume, and $\Omega(z, \log L)$ the area curve of the survey.

Since X-ray counts and background counts are not available for all sources in our sample, we treat X-ray fluxes as delta functions. Hence, the uncertainties in Eq. (19) reduce to the uncertainties on the redshift estimation. In a similar fashion to Aird et al. (2010), we introduce the full probability distribution function of the photometric redshift estimates in our computation. The photometric redshifts in our sample (XMM-COSMOS, LH, XMM-CDFS, and AEGIS-XD) were computed in a consistent way with special treatment for AGN, i.e., including hybrid templates and applying proper prior information on the absolute magnitude as defined in Salvato et al. (2011).

We use noninformative distributions of priors for all parameters. The expected range for each parameter is determined from previous works on the AGN luminosity function in the 2–10 keV band, however, we do not wish to assume any shape for the distribution of the parameters.

To perform Bayesian analysis, we used MultiNest (Feroz & Hobson 2008; Feroz et al. 2009, 2013) through its python wrapper PyMultiNest⁵ (Buchner et al. 2014). MultiNest performs Nested Sampling introduced by Skilling et al. (2004) and is able to explore the posterior even in the case of multimodal distributions.

In Fig. 4 we plot the residuals between the model prediction and observed data for all models $(N_{\text{model}} - N_{\text{data}})/N_{\text{data}}$. All models are able to reproduce the total number of AGN observed (1105 objects available with redshift in our sample), albeit with about 40–50% uncertainty at 90% level. For each model, we also

³ Kelly et al. (2008) provide an in-depth discussion on the Bayesian analysis of the luminosity function using a binomial distribution.

⁴ Hereafter we use the symbol \mathcal{L} to represent in the likelihood instead of $p(D|\theta, M)$ to be consistent with XLF literature.

⁵ <https://github.com/JohannesBuchner/PyMultiNest>

Table 2. Model selection criteria.

	LDDE	Ueda14	PLE	LADE	PDE	ILDE
k	9	15	7	8	7	6
Δ AIC	0	13	41	37	150	269
Δ BIC	0	43	31	32	140	254

Notes. According to AIC and BIC, LDDE is the preferred model.

show the distribution in redshift (top panels) and in luminosity (right-hand panels). The gray histogram is the distribution of the observed data, while the solid black line is the prediction of each model. The redshift histograms indicate that the models do not capture the redshift spikes observed around $z = 0.6$ and $z = 1.0$. At low redshifts ($z < 0.3$) we see that only the models LDDE and Ueda14 correctly capture the local luminosity function. LDDE best reproduces the one-dimensional distributions in redshift and luminosity and, at the same time, the two-dimensional representation, while Ueda14 shows a suppression in the predicted number of sources. At low redshift, both LADE and PLE show an underestimated number of sources close to $\log L_x = 43$ and an overestimated number of sources at low ($\log L_x = 42$) and high ($\log L_x = 44$) luminosities. Lastly, models PDE and ILDE appear unable to capture the change in number of AGN showing large islands of under- and overestimation of the number of AGN both at low and high redshifts.

4.2. Model selection

We apply the following two tests to identify the model that describes our dataset best.

Akaike information criterion (AIC). The AIC selects the model with the least information loss, penalizing models with a higher number of free parameters (Akaike 1974). Therefore, it incorporates the Occam’s razor, which among two equally plausible explanations prefers the simpler explanation. The AIC is computed as

$$\text{AIC} = 2k - 2 \ln \mathcal{L}, \quad (20)$$

where k is the number of parameters present in the model and \mathcal{L} the maximum likelihood value. The preferred model is that with the lowest AIC value.

Bayesian information criterion (BIC). The BIC selects models according to their likelihood value computed in a similar fashion to AIC, but with a higher penalty for complicated models (Schwarz 1978). It is expressed as

$$\text{BIC} = k \cdot \ln n - 2 \ln \mathcal{L}, \quad (21)$$

where k is the number of parameters of the model and n is the number of observations. The preferred model is that with the lowest BIC value. Models with difference less than six must also be considered.

In Table 2 we give the comparison between LDDE and all other models. Both AIC and BIC identify the LDDE as the preferred model. For the dataset considered in this work, both selection criteria point to the direction that no other model can serve as an alternative. We see that according to the model selection criteria, ILDE is the worst representation; see Sect. 4.1

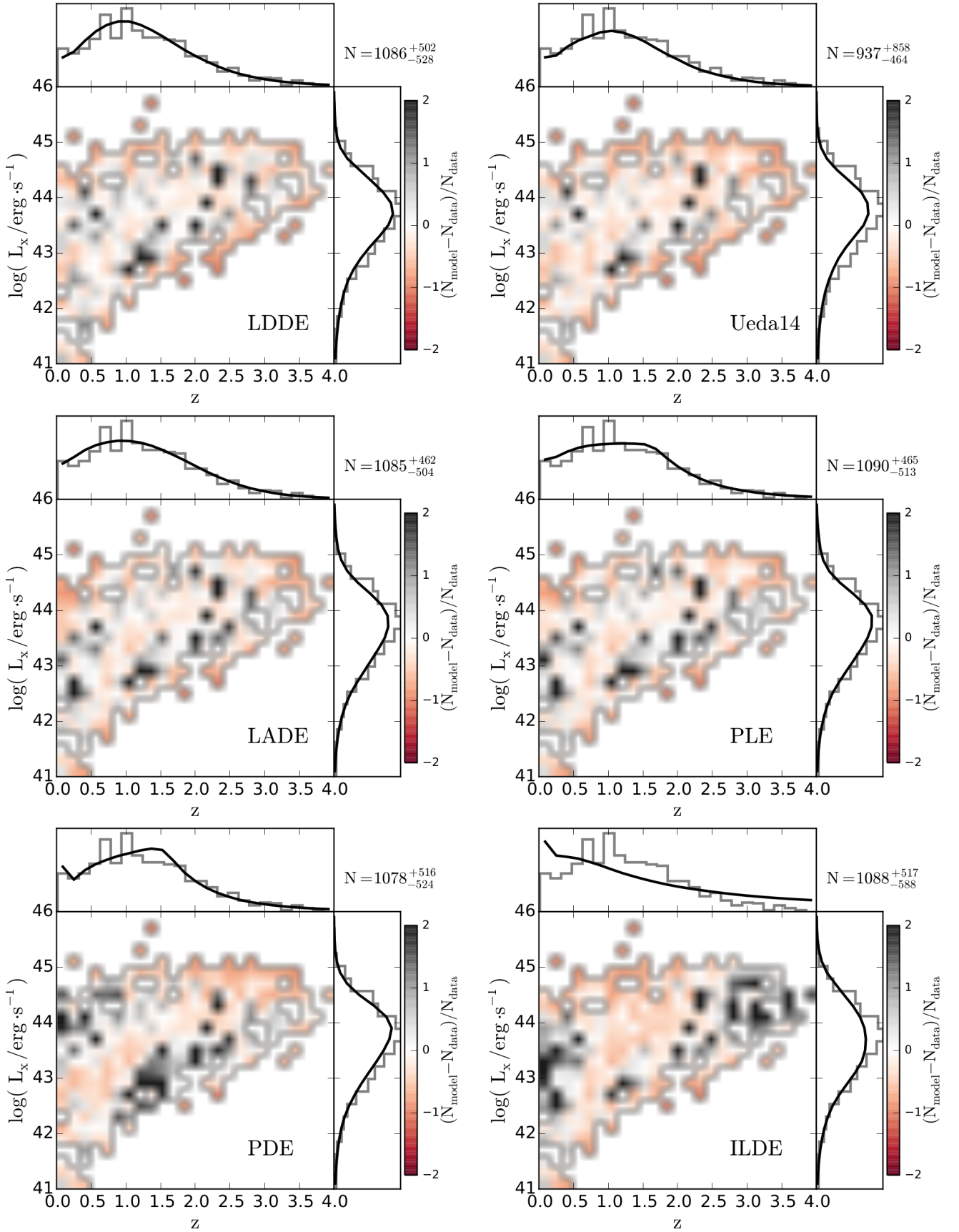


Fig. 4. Fractional difference between predicted and observed number of AGN in a luminosity-redshift bin (color scale). The computation of the volume and luminosity function was performed on a 1000×1000 grid. The plots are rebinned on a 25×25 grid. *Top and right-hand panels* show the distribution in redshift and luminosity, respectively. The histograms represent the data, while the black lines are the model estimation.

Table 3. LDDE parameter summary.

Parameter	Prior interval		Posterior mode		
			mean	standard deviation	
$\log L_0$	41.0	–	46.0	43.77	0.11
γ_1	–2.0	–	5.0	0.87	0.06
γ_2	–2.0	–	5.0	2.40	0.11
p_1	0.0	–	10.0	5.89	0.31
p_2	–10.0	–	3.0	–2.30	0.50
z_c	0.01	–	4.0	2.12	0.16
$\log L_a$	41.0	–	46.0	44.51	0.11
α	0.0	–	1.0	0.24	0.02
$\log A$	–10.0	–	–2.0	–5.97	0.17

Notes. We recommend the use of posterior draws sampled with MultiNest; available upon request.

(Fig. 4). From the simpler models, PDE performs worst than PLE. Additionally, we see that LADE, which allows an independent evolution in luminosity and number density, is comparable PLE. Since BIC includes 15 model parameters, it imposes a strong penalty on the LDDE formalism of Ueda et al. (2014).

4.3. Results

In Table 3 we summarize the parameter estimation of the LDDE model. We report the uniform prior interval and the posterior mean and standard deviation for each parameter. From Eq. (1) we can see that parameters γ_1 and γ_2 are symmetric, which means that the posterior distribution contains two modes. These two modes are easily distinguished with MultiNest and summary statistics are provided for each mode (see also Sect. 5.1).

In Fig. 5 we plot the differential luminosity function for several redshift bins. The solid black line shows the peak of the distribution of the luminosity function at the median redshift of each redshift bin, while the gray shaded area encloses 90% probability of the differential luminosity function, $d\phi/d\log L_x$. To determine this area, we compute $d\phi/d\log L_x$ in each redshift bin for 40 values of the luminosity, L_x , for all the draws from the posterior. In this way, we naturally incorporate the true shape of the uncertainties for all parameters and their covariances. For reference, the dashed black line shows the luminosity function computed at redshift zero, using our model parameters in Eq. (1). The two (overlapping) red lines show the luminosity function when mode 1 and mode 2 are considered separately. As expected and demonstrated in Fig. 5, the estimation of the LF is better constrained in the $(L-z)$ locus where observations are available and less constrained when extrapolating⁶.

The black points are the result of the $1/V_{\max}$ method. The $1/V_{\max}$ method (Schmidt 1968) has been used widely in the literature to estimate the luminosity function of AGN. The advantage of this method is that the estimation is independent of any assumption on the underlying model. When a sizable sample of AGN is used, the computation of the luminosity function in thin redshift bins is powerful in revealing the presence of evolution. This computation also roughly reveals the shape of the XLF. Here we use the estimator proposed by Page & Carrera (2000)

$$\frac{d\phi(L, z)}{d \log L} = \frac{n}{\int_{\log L_{\min}}^{\log L_{\max}} \int_{z_{\min}}^{z_{\max}(L)} \Omega(z, \log L) \frac{dV}{dz} dz d \log L}, \quad (22)$$

⁶ Assuming that the parameters are independent results in a large over-estimation of the uncertainties on the luminosity function.

where n is the number of AGN in the bin $[L_{\min}, L_{\max}]$, and $[z_{\min}, z_{\max}(L)]$. The value $z_{\max}(L)$ corresponds to the maximum redshift up to which the n sources would be still present in the sample, and this value is either the maximum redshift of the redshift bin or is given by the flux limit. Since it is a model independent method, it serves as a check for our fitting result.

5. Discussion

5.1. Information per survey

In Fig. 6 we show the marginal posterior distribution of each parameter for the LDDE model. The gray shaded area represents the XLF parameter distribution when we take all of the surveys we used into account. The colored lines represent the LDDE parameters estimated from each survey independently. In a maximum likelihood estimation, a method commonly used in previous works, one would be forced to fix one or more evolutionary parameters to gain some perspective on the local luminosity function when using a shallow survey such as MAXI. One of the advantages of our analysis is exploring the posterior without having to assume any specific shape for the likelihood. All parameters are left free and any dataset can be used to extract information, even for complicated models. For example, as seen in Fig. 6 MAXI (green) and HBSS (light blue) carry essentially no information about L_a , and a . Therefore, the marginal distribution for these parameters has the same shape as the prior, which in our case was a flat distribution. On the other hand, the deepest fields AEGIS-XD (red), and XMM-CDFS (black) are able to put constraints on the evolution parameters.

We can quantify the information gained and encoded in the posterior distribution compared to the prior information using the Kullback-Leibler divergence (Kullback & Leibler 1951)

$$D_{\text{KL}}(P||Q) = \int_{-\infty}^{+\infty} p(x) \log_2 \frac{p(x)}{q(x)} dx, \quad (23)$$

where P and Q are two continuous random variables and p, q are their corresponding probability density functions. The information gain is measured in bits since the logarithm with base 2 is used⁷. In Table 4 we show the information gain per survey and for combinations of surveys. In general, the shallow surveys provide higher information content on the LDDE parameters that describe the local XLF ($\log L_0, \gamma_1, \gamma_2$) and the overall normalization (A). On the other hand, deep surveys provide information on the evolution of the XLF with redshift (p_1, p_2). The luminosity dependence of the density evolution is constrained by the deepest fields, LH and AEGIS. The only field that does not conform to the expectation is *Chandra*-CDFS from which we find information gain for all model parameters, apart from parameter α .

Both astrophysical and systematic effects contribute to differences observed in the information present in each survey. Astrophysical effects include cosmic variance due to the presence of structures (e.g., clusters of galaxies), which would affect most the small-area fields (LH, XMM-CDFS, AEGIS). Also, because of the trade-off between depth and area covered by each survey, there is a lack of low-luminosity sources at higher redshifts. If a certain population (type I vs. II, or highly obscured AGN) is dominant at specific redshifts, this would

⁷ One bit corresponds to the reduction of the standard deviation of a Gaussian distribution by a factor of three: http://www.mpe.mpg.de/~jbuchner/bayes/utility/singlegauss_bits.xhtml

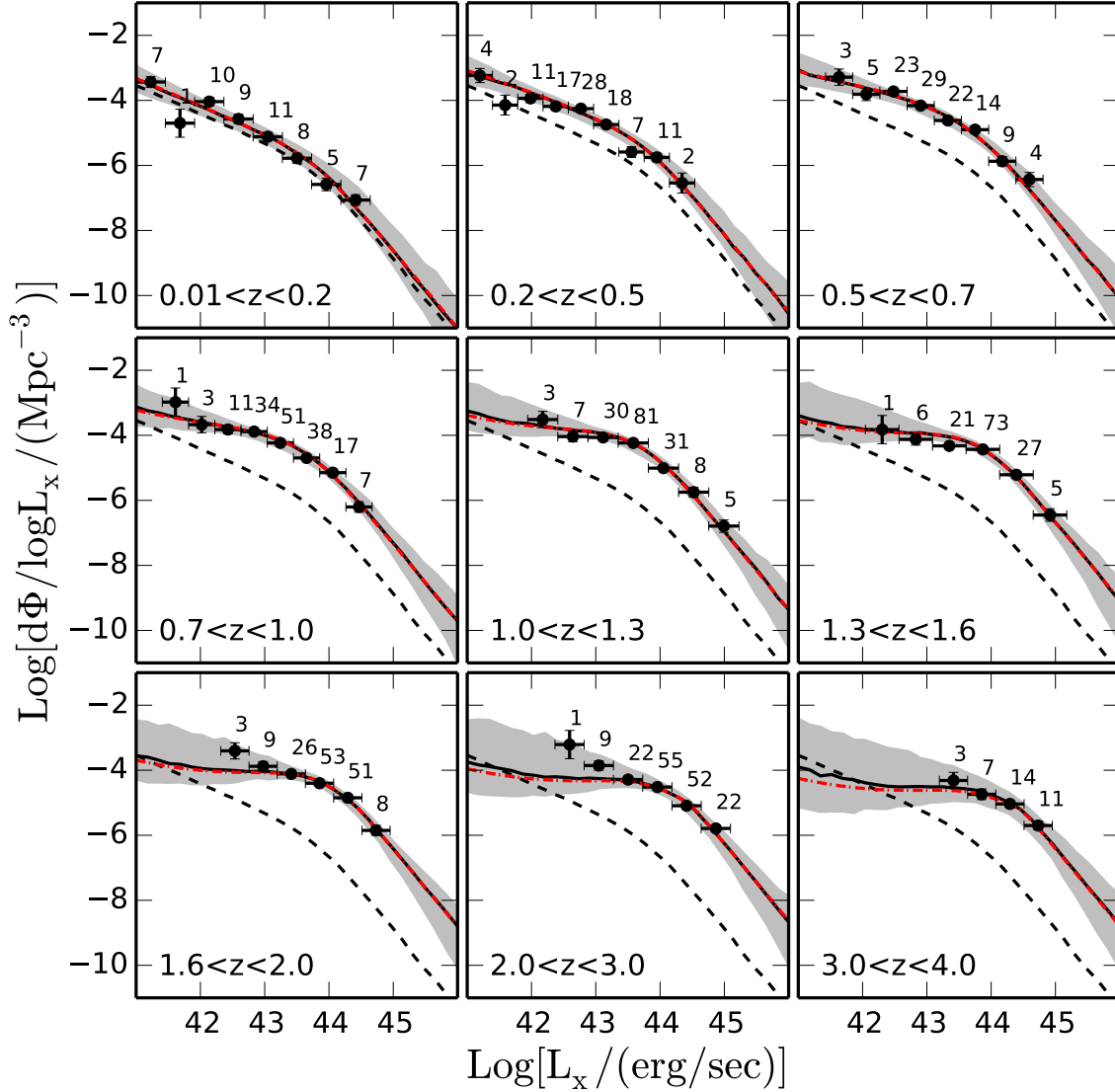


Fig. 5. Differential luminosity function versus luminosity for different redshift bins. The number of sources in each bin is given on the top right of each point. The solid black line is the mode of the luminosity function distribution, the gray shaded area encloses the 99% credible interval. The dashed black line shows the estimated luminosity function at $z = 0$ for comparison. The two red lines show the estimated luminosity function when the two posterior modes are used separately. The points are the binned estimations of the luminosity function, according to the $1/V_{\max}$ method, and they are in excellent agreement with our model.

bias our result. The biases introduced by astrophysical effects are effectively conquered by the combination of independent surveys.

Ideally, all data should be extracted in a homogeneous manner, but for technical reasons this is not always possible. Therefore, differences due to systematic effects include: 1) deviations in the calibration of the X-ray satellites; for instance, [Lumb et al. \(2001\)](#) and [Tsujiimoto et al. \(2011\)](#) reported a 10–20% difference in flux between *XMM-Newton* and *Chandra*; 2) difference in adopted survey detection limits determining the inclusion or not of a source in the catalog, which also affects the determination of the area curve of the survey; and 3) assumptions on the power-law index when converting counts to fluxes and fluxes to luminosities. We tested the latter for the AEGIS-XD survey, comparing the evidence between $\Gamma = 1.4$ and $\Gamma = 1.9$. We find no difference in the preferred model in the two cases. The bottom panel of [Table 4](#) shows the information gain when the surveys are considered in a coherent

way ([Avni & Bahcall 1980](#)). The combination of all XMM surveys provides enough information to constrain the behavior of the XLF at high redshifts through the model parameters $\log L_{\alpha}$ and α . The *Chandra* surveys we consider cover a smaller area compared to the XMM surveys, but they are deeper than the XMM surveys. Runs 9 and 10 show the information gained when using only XMM surveys and only *Chandra* surveys, respectively. The parameter p_1 , which describes the evolution of the XLF below the critical redshift z_c , is constrained better by the XMM surveys, while the high redshift evolution is constrained better by *Chandra*. In [Table 5](#) we give the best-fit parameters for runs 9–14. There is notable difference between XMM-only and *Chandra*-only surveys. As seen from the information gain analysis, XMM surveys do constrain the high redshift evolution but with large uncertainties (20% on parameter α). On the other hand, *Chandra*-only fields lead to a somewhat biased estimation of the XLF evolution at low redshift (parameter $p_1 \approx 7$). The reason for this discrepancy is the result of the area covered by

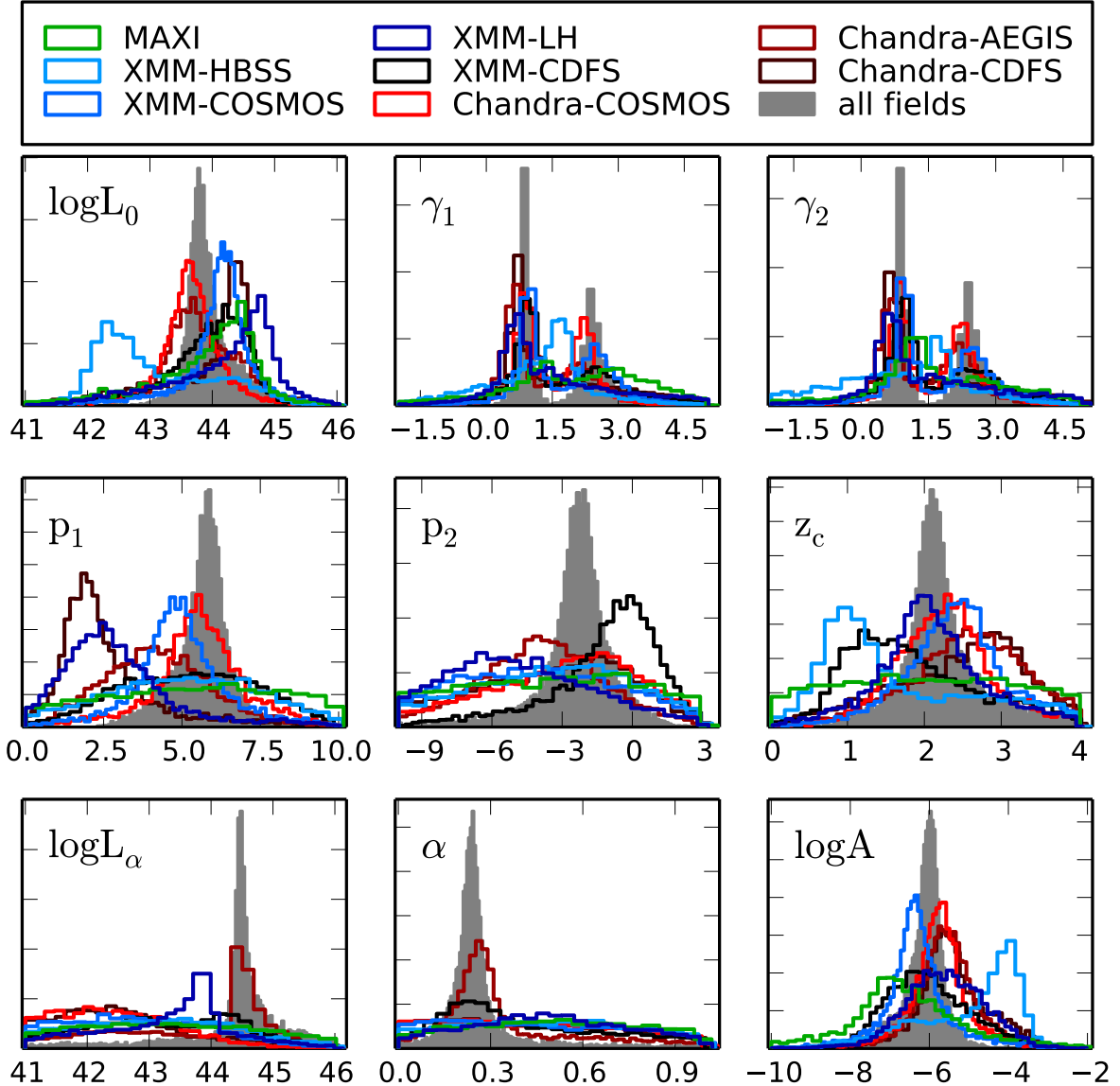


Fig. 6. Marginal probability distribution function for LDDE parameters per survey. The gray shaded area shows the distribution of the parameters when all the fields are considered. The colored lines show the luminosity function parameters determined separately in each field. Flat distribution means that no information is present in a given survey about a particular model parameter.

the *Chandra* surveys, and not the result of systematic differences between the two instruments. At high redshift, both XMM and *Chandra* surveys converge to the same parameter estimation. The introduction of the MAXI survey significantly enhances the estimated XLF parameters, as seen by the information gained in Table 4.

5.2. Luminosity function evolution

Previous works in the 2–10 keV band have shown that the evolution of the AGN luminosity function is best described by the LDDE model (Ueda et al. 2003, 2014; La Franca et al. 2005; Silverman et al. 2008; Ebrero et al. 2009; Yencho et al. 2009; Miyaji et al. 2015; Aird et al. 2015). The comparison among these works and the work presented here is not straightforward, as the sample selection and treatment vary. For example, each work treats corrections for intrinsic absorption and corrections for redshift incompleteness differently. Additionally, not

all models are tested in the literature for compliance with each dataset, and the most commonly used are the PLE and LDDE models.

With this work we treat most of the analysis shortcomings found in earlier literature. We take photometric redshift uncertainties for all sources into account, assuming a flat redshift probability distribution between $z = 0-7$ for sources with no redshift estimation. As discussed in Sect. 5.1, we do not fix any of the evolutionary parameters, since it is not needed within the Bayesian framework adopted for our analysis. Also, the 5–10 keV energy band chosen allows us to estimate the luminosity function of AGN, avoiding assumptions about the obscuration based on hardness ratios that could lead to a biased estimation of the absorbing column density (Brightman & Nandra 2012).

In Fig. 7a we provide a visualization of the MultiNest draws for our best model (black points). There are significant correlations between the model parameters that must not be neglected

Table 4. Prior-posterior information gain measured in bits on the marginal distribution of each model parameter.

Run	Field selection			Information gain (bit)								
				$\log L_0$	γ_1	γ_2	p_1	p_2	z_c	$\log L_\alpha$	α	$\log A$
1	MAXI			0.67	0.26	0.40	0.04	0.03	0.02	0.05	0.04	0.53
2	XMM-HBSS			0.54	0.66	0.38	0.13	0.10	0.30	0.13	0.04	0.76
3	XMM-COSMOS			1.23	0.97	0.92	0.77	0.08	0.59	0.23	0.04	1.27
4	XMM-LH			0.65	0.58	0.54	0.66	0.19	0.52	0.39	0.09	0.94
5	XMM-CDFS			0.92	0.74	0.73	0.24	0.59	0.31	0.16	0.18	0.9
6	<i>Chandra</i> -COSMOS			1.26	1.2	1.08	0.73	0.16	0.63	0.47	0.05	1.38
7	<i>Chandra</i> -AEGIS-XD			0.88	0.79	0.93	0.50	0.31	0.40	0.41	0.60	1.28
8	<i>Chandra</i> -CDFS			0.83	0.72	0.68	0.91	0.13	0.28	0.35	0.05	1.13
9	–	XMM	–	1.54	1.22	1.40	1.17	0.53	0.74	0.35	0.58	1.63
10	–	–	<i>Chandra</i>	1.51	1.34	1.24	0.35	0.89	0.83	0.63	0.95	1.91
11*	–	XMM	<i>Chandra</i>	1.81	1.52	1.57	1.10	1.02	0.97	0.87	1.25	2.09
12	MAXI	XMM	–	1.65	1.33	1.29	1.59	0.58	0.74	0.38	0.71	1.67
13	MAXI	–	<i>Chandra</i>	1.63	1.39	1.31	1.31	1.09	0.74	0.78	1.27	1.82
14*	MAXI	XMM	<i>Chandra</i>	1.88	1.57	1.52	1.59	1.15	1.01	1.04	1.53	2.02

Notes. Zero bits means that the dataset carried no information regarding the specific parameter. (*) In the runs where both XMM and *Chandra* fields are used, the overlap of the COSMOS and CDFS fields have been taken into account, as described in Sect. 2.1.

Table 5. LDDE parameter summary for runs 9–14.

Parameter	XMM	<i>Chandra</i>	XMM+ <i>Chandra</i>	MAXI+XMM	MAXI+ <i>Chandra</i>	MAXI+XMM+ <i>Chandra</i>
$\log L_0$	43.97 ± 0.19	43.62 ± 0.14	43.72 ± 0.12	44.04 ± 0.15	43.77 ± 0.13	43.77 ± 0.11
γ_1	0.97 ± 0.07	0.92 ± 0.09	0.86 ± 0.06	0.99 ± 0.07	0.86 ± 0.06	0.87 ± 0.06
γ_2	2.53 ± 0.22	2.46 ± 0.17	2.37 ± 0.11	2.65 ± 0.22	2.43 ± 0.16	2.40 ± 0.11
p_1	5.72 ± 0.51	7.02 ± 0.93	6.03 ± 0.45	5.72 ± 0.36	5.92 ± 0.38	5.89 ± 0.31
p_2	-2.72 ± 1.14	-1.81 ± 0.56	-2.19 ± 0.54	-2.72 ± 1.07	-2.19 ± 0.56	-2.30 ± 0.50
z_c	2.19 ± 0.35	1.99 ± 0.21	2.08 ± 0.17	2.28 ± 0.36	2.15 ± 0.25	2.12 ± 0.16
$\log L_\alpha$	44.55 ± 0.34	44.48 ± 0.10	44.49 ± 0.11	44.68 ± 0.34	44.53 ± 0.17	44.51 ± 0.11
α	0.26 ± 0.05	0.26 ± 0.03	0.25 ± 0.02	0.24 ± 0.04	0.24 ± 0.02	0.24 ± 0.02
$\log A$	-6.26 ± 0.28	-6.04 ± 0.24	-5.92 ± 0.18	-6.38 ± 0.24	-5.98 ± 0.20	-5.97 ± 0.17

during the model parameter estimation, for example, by fixing model parameters. We also plot on the same figure the best parameter point estimates of Ueda et al. (2014) (blue), Miyaji et al. (2015) (green), and Aird et al. (2015) (red). We see that all model estimations agree on the break luminosity $\log L_0$, the normalization and high redshift z_c evolution given by $\log L_\alpha$ and α parameters. On the other hand, there is disagreement on the slopes of the XLF and their evolution with redshift. The surveys we use for all of the analyses contain strong evidence to constrain the break points in the XLF model, namely $\log L_0$, z_c , $\log L_\alpha$. The exact shape, however, depends upon the quality of the redshift measurement, spec- z vs. photo- z , and if the full PDF is taken into account. Additionally, the presence of absorption is an extra modeling factor that can introduce bias in the estimation of the XLF. By selecting objects in the 5–10 keV energy band, we remove the effects of this extra set of model assumptions.

In Fig. 7b we show our result transformed to the 2–10 keV energy band assuming AGN spectra can be described by a power law with $\Gamma = 1.9$ (black solid line, dark gray area: 90% credible interval) and recent results from the literature (magenta,

Hopkins et al. 2007; blue, Ueda et al. 2014; green, Miyaji et al. 2015; yellow, Buchner et al. 2015; red, Aird et al. 2015) for four redshift intervals. There is a remarkable agreement between all results up to redshift 2.5, and any small deviations are within the uncertainties.

Despite the many efforts of deep X-ray programs, the AGN XLF above $z = 3$ is still under debate. Brusa et al. (2009) noted that the high redshift number density of AGN in the XMM-COSMOS field showed a decline that is more rapid than the predictions of the XLF models. The same trend was found in the *Chandra*-COSMOS observations by Civano et al. (2011). In the last panel of Fig. 7 ($z = 3.6$) we plot two more literature results from Vito et al. (2014) (thin black line) and Georgakakis et al. (2015) (thin gray line). Both works provide a parametric model estimation of the AGN XLF at $3 < z < 5$. We see that the estimates cluster in two regimes: a significant drop in the number density (Miyaji et al. 2015; Aird et al. 2015; Georgakakis et al. 2015) and a shallower drop in the number density (Hopkins et al. 2007; Ueda et al. 2014; Vito et al. 2014; Buchner et al. 2015). Our work is in agreement with the latter group and especially

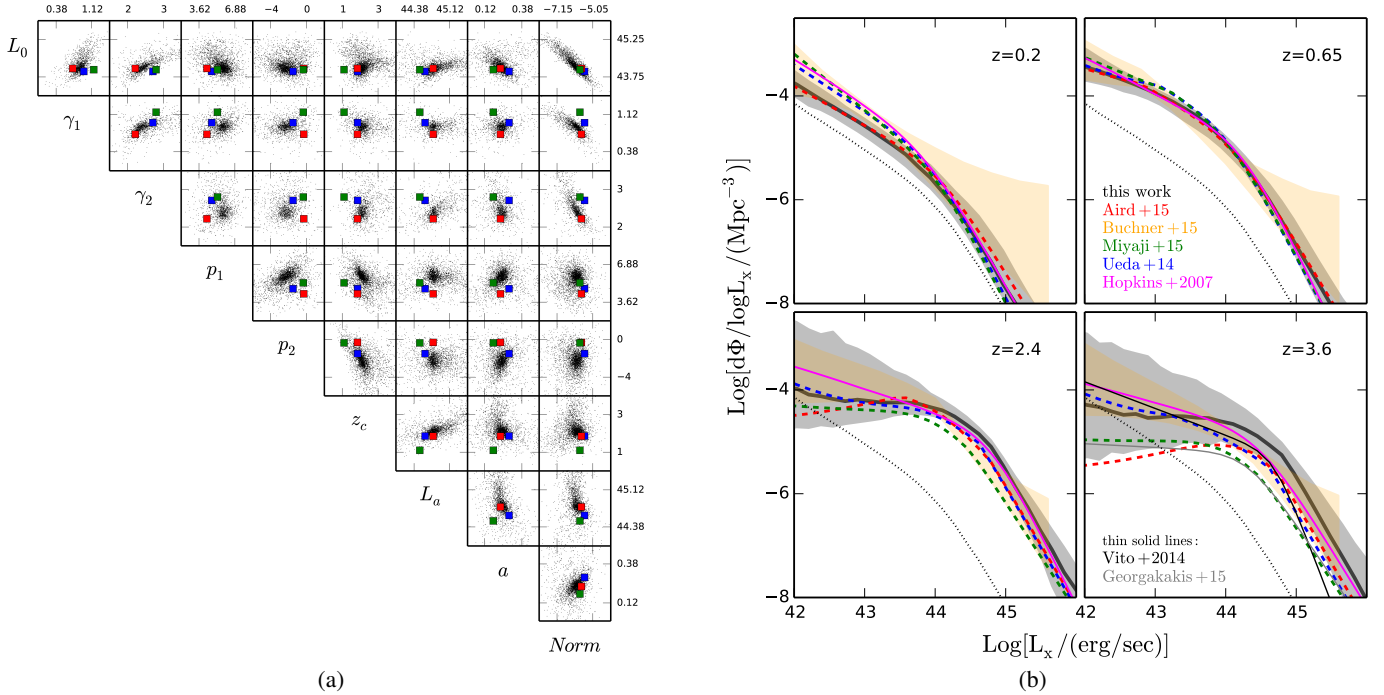


Fig. 7. **a)** Posterior draws from MultiNest (black) and comparison with the point estimates from Ueda et al. (2014) (blue), Miyaji et al. (2015) (green), Aird et al. (2015) (red). **b)** Comparison of 5–10 keV luminosity function (black line) transformed to 2–10 keV to literature results. The gray area shows the 90% credible interval. Our result is in excellent agreement with the literature up to $z = 2.5$. At high redshift our result shows a less prominent drop in the faint end of the XLF compared to estimations from Miyaji et al. (2015) (green), Aird et al. (2015) (red), and Georgakakis et al. (2015) (thin black line).

with the novel nonparametric XLF estimate of Buchner et al. (2015). Even though Ueda et al. (2014) proposed a more complicated formalism for the LDDE model to take the change of the AGN number density at $z > 3$ into account, our work shows that at least up to redshift four, there are a set of model parameters able to describe the AGN XLF without introducing extra complexity in the LDDE model.

5.3. AGN number density

In Fig. 8 we plot the number density as a function of redshift for three luminosity bins. Our dataset shows the antihierarchical growth of black holes that has been observed previously in soft (0.5–2 keV) and hard (2–10 keV) energy bands. At the brightest luminosity range ($44 < \log L_x < 45$), the number density for this dataset shows more of a flattening than a drop, in contrast to the estimations of Brusa et al. (2009), Civano et al. (2011), and Kalfountzou et al. (2014). Ueda et al. (2014) fix their second critical redshift at $z = 3$. Miyaji et al. (2015) use a sample of 3200 AGN in the 2–10 keV band and demonstrate that a second break is present between $z = 2$ –3 after which a decline in the number density is observed. Our dataset is not numerous enough at $z > 3$ to support a more complicated evolution for AGN.

The antihierarchical growth of supermassive black holes, as imprinted on the AGN luminosity function, might seemingly be in stark contrast with the hierarchical structure formation within the framework of Λ CDM cosmology. Through hydrodynamic simulations and semi-analytic modeling, it has been shown that it is possible to qualitatively reconcile structure formation and AGN activity. Nevertheless, semi-analytic models are not able to rule out AGN evolutionary models or pinpoint the exact mechanism behind downsizing at this stage. Still largely debated in

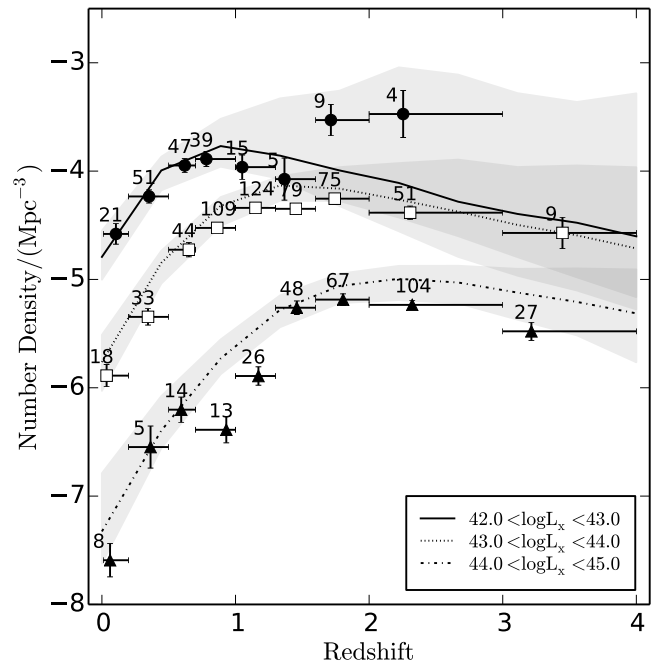


Fig. 8. Number density as a function of redshift for three luminosity bins showing the antihierarchical growth of black holes. The number of AGN per bin are given above each point.

the literature, the predicted AGN luminosity function, from hydrodynamic simulation and semi-analytic modeling, is subject to the adopted AGN light curve and lifetime, obscuration, triggering mechanism, and feedback.

For example, in Fanidakis et al. (2011) the authors assumed that accretion takes place in two distinct modes, radiatively efficient and radiatively inefficient mode. Combining their semi-analytical model with the obscuration prescription from Hasinger (2008), they show that the bright end of the luminosity function is populated by quasars emitting close to the Eddington limit, while the faint end of the luminosity function is populated by black holes that undergo quiescent accretion. Hirschmann et al. (2014) showed that their hydrodynamic simulation is able to reproduce the observed downsizing at redshifts $z = 0-5$, also allowing for cold gas accretion and major mergers. These authors mainly attribute the observed behavior to the gas density in the vicinity of the black hole, and they find the evolution of the gas reservoir was a consequence of star formation and AGN feedback. They also allow for obscuration in their models, following Hasinger (2008).

Even though dust obscuration can clearly enhance the observed flattening of the faint end of the luminosity function, which is particularly true for the soft X-ray band, the fact that downsizing is also observed in the 5–10 keV band, where the effect of the obscuration is minimal, points to the fact that this is not the predominant factor that shapes the AGN luminosity function. Hopkins et al. (2006) interpreted the AGN luminosity function in terms of quasar lifetimes and found good agreement between their simulations and the LDDE model, i.e., flattening of the faint end of the luminosity function. They claim that the observed break in the luminosity function corresponds to the maximum of the peak luminosity distributions of quasars at a certain redshift. The bright end of the luminosity function is populated by quasars that emit at their peak luminosity, while the faint end is populated by quasars that emit at lower luminosities. In their modeling, quasars spend the majority of their lifetime below their peak luminosity while, at the same time, more luminous objects transit to a less luminous stage faster than objects with lower peak luminosity. This implies that the slope of the faint end of the luminosity function is flatter at higher redshift. More recently, Enoki et al. (2014), assuming only major merger driven AGN triggering and no obscuration effects, showed that a combination of parameters could reproduce the observed downsizing: 1) cold gas depletion due to star formation; 2) scaling of the AGN lifetime with the dynamical time, in which high redshift AGN has a shorter dynamical time; and 3) suppression of gas cooling in massive dark matter halos.

5.4. Future surveys

With an anticipated detection of millions of AGN in the 0.5–2 keV energy range at a flux limit of $f_{0.5-2\text{keV}} = 10^{-14} \text{ erg s}^{-1} \text{ cm}^{-2}$, eROSITA will mark a new era in the study of AGN. Over the 2–10 keV energy range, the brighter flux limit of $f_{2-10\text{keV}} = 4 \times 10^{-14} \text{ erg s}^{-1} \text{ cm}^{-2}$ will allow the detection of hundreds of thousands of AGN (Merloni et al. 2012).

Transforming our 5–10 keV luminosity function in the 2–10 keV energy band and assuming an unabsorbed power law with photon index $\Gamma = 1.9$, we predict a total of 1.8×10^5 unabsorbed AGN in the range $0.01 < z < 4$ and $41 < \log L_x < 46$, assuming 80% of the sky is accessible. This number is in good agreement with the prediction of Kolodzig et al. (2013), which anticipated 130 000 AGN in the four-year survey over $34\,100 \text{ deg}^2$. In Fig. 9 (black contours) we show the expected number of AGN detected with eROSITA. The coverage of the L_x - z plane will not be homogenous, and the majority of the detected sources are close to the break of

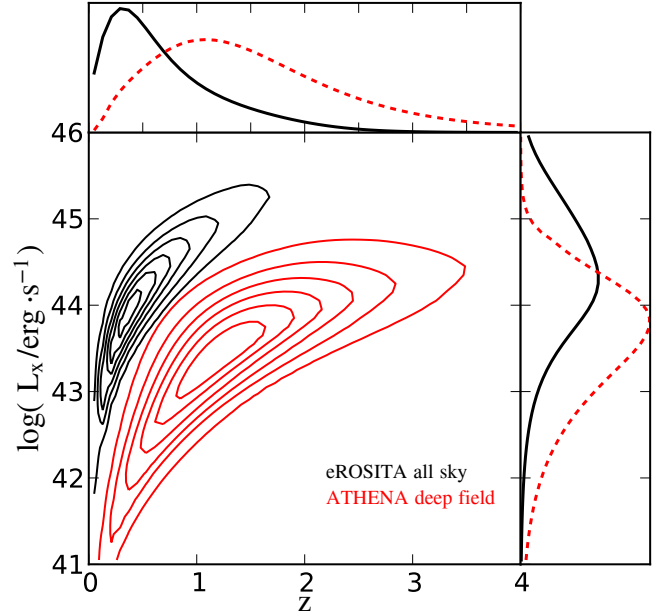


Fig. 9. Expected luminosity-redshift plane coverage from the all-sky survey with eROSITA (black curves) and ATHENA (red curves) in the 2–10 keV energy band. *Top panel* shows the predicted redshift distribution. Panel on the *right* shows the predicted luminosity distribution. The two missions complement each other and both are pivotal for a precise estimation of the AGN luminosity function.

the luminosity function at redshift 0.5. The eROSITA all-sky survey will measure the local luminosity function of AGN and its evolution up to $z = 1$. At higher redshifts, constraints on the bright end of the luminosity function will be possible. The top and right-hand histograms show the expected number distributions of AGN in redshift and luminosity, respectively.

To determine the behavior of the AGN number density during the golden era of quasars at a comparable quality level to the sample provided by eROSITA, wide *and* deep surveys are needed. The ATHENA mission will be able to provide such observations. The red contours in Fig. 9 show the expected number of AGN from ATHENA, assuming the multitiered survey strategy described in Aird et al. (2013) and Georgakakis et al. (2013), reaching a flux limit of $f_{2-10\text{keV}} = 8 \times 10^{-17} \text{ erg s}^{-1} \text{ cm}^{-2}$ in the deepest area. The total anticipated number of AGN according to our model is 2.8×10^5 AGN in the redshift range $0 < z < 4$ and 8×10^4 AGN in the redshift range $1 < z < 2$, which is below the break luminosity $\log L_x < 44$. With the combination of these unprecedented samples of AGN, we will be able to provide the most accurate constraints on the luminosity function and its evolution.

6. Conclusions

Combining the most recent X-ray observations from MAXI, HBSS, XMM-COSMOS, XMM-LH, XMM-CDFS, *Chandra*-COSMOS, *Chandra*-AEGIS-XD, and *Chandra*-CDFS in the 5–10 keV energy band, we compile a sample of 1100 AGN with 98% redshift completeness. We use the *Chandra* data in the inner region of the COSMOS and CDFS fields, and the *XMM-Newton* data in the outskirts where no *Chandra* data are available, to profit both from the depth and breadth of the observations. Our sample contains 68% spectroscopic redshifts and 30% very accurate photometric redshifts estimations

from the fields XMM-COSMOS, XMM-LH, XMM-CDFS, *Chandra*-AEGIS-XD, *Chandra*-COSMOS, and *Chandra*-CDFS. Studying the 5–10 keV energy range, we avoid the potentially absorbed part of the spectrum for common N_{H} values, effectively avoiding any assumption on otherwise necessary corrections to retrieve intrinsic X-ray luminosities.

Using Bayesian analysis we estimate the AGN 5–10 keV luminosity function and its evolution with redshift. Our results strongly support the LDDE model compared to PLE, PDE, LADE, and ILDE. We have demonstrated that by exploring the likelihood via MultiNest, we no longer need to fix model parameters even when there is not enough information in a dataset to constrain a complicated model. We quantify the information gain per XLF model parameter for the LDDE model for each individual field and for XMM and/or *Chandra* field combinations. We show that the evolution predicted by XMM-only and *Chandra*-only fields is varying, but this evolution remains consistent within the uncertainties at the 90% level.

We rule out the possibility of a pure density evolution. Our results demonstrate the presence of one critical redshift after which the evolution changes behavior and shows no evidence of a second critical redshift up to redshift four. Future work should focus on physically motivated evolutionary models, coupling the observed change in number density with AGN physics. We rule out the possibility of obscuration as the primary explanation for the observed antihierarchical growth of AGN.

Planned X-ray observatories will give an unprecedented view of the bright end of the luminosity function. We predict 1.8×10^5 AGN up to $z = 4$ in the four-year, all-sky survey with eROSITA, while the multitiered survey strategy with ATHENA proposed in Aird et al. (2013) would provide the outstanding number of 10^4 AGN at $1 < z < 2$ and $\log L_x < 44$, which is sufficient to study the *golden era* of quasars and their coevolution with galaxies.

Acknowledgements. S.F. acknowledges a grant from the Swiss National Science Foundation. This work benefited from the THALES project 383549, which is jointly funded by the European Union and the Greek Government in the framework of the program “Education and lifelong learning”. Financial contribution from the agreement ASI-INAF I/009/10/0 and “PRIN-INAF 2011” is acknowledged. M.B. acknowledges support from the FP7 Career Integration Grant “eEASy” (“SMBH evolution through cosmic time: from current surveys to eROSITA-Euclid AGN Synergies”, CIG 321913). T.M. is supported by UNAM DGAPA Grant PAPIIT IN104113 and CONACyT Grant 179662.

References

- Aird, J., Nandra, K., Laird, E. S., et al. 2010, *MNRAS*, 401, 2531
- Aird, J., Comastri, A., Brusa, M., et al. 2013, ArXiv e-prints [arXiv:1306.2325]
- Aird, J., Coil, A. L., Georgakakis, A., et al. 2015, *MNRAS*, 451, 1892
- Akaike, H. 1974, *IEEE Transactions on Automatic Control*, 19, 716
- Akylas, A., Georgakakis, A., Georgantopoulos, I., Brightman, M., & Nandra, K. 2012, *A&A*, 546, A98
- Antonucci, R. 1993, *ARA&A*, 31, 473
- Arnaud, K. A. 1996, *Astronomical Data Analysis Software and Systems V*, 101, 17
- Avni, Y., & Bahcall, J. N. 1980, *ApJ*, 235, 694
- Ballantyne, D. R., & Papovich, C. 2007, *ApJ*, 660, 988
- Barro, G., Pérez-González, P. G., Gallego, J., et al. 2011a, *ApJS*, 193, 13
- Barro, G., Pérez-González, P. G., Gallego, J., et al. 2011b, *ApJS*, 193, 30
- Beckmann, V., Soldi, S., Shrader, C. R., Gehrels, N., & Produit, N. 2006, *ApJ*, 652, 126
- Boyle, B. J., Shanks, T., Georgantopoulos, I., Stewart, G. C., & Griffiths, R. E. 1994, *MNRAS*, 271, 639
- Buchner, J., Georgakakis, A., Nandra, K., et al. 2014, *A&A*, 564, A125
- Buchner, J., Georgakakis, A., Nandra, K., et al. 2015, *ApJ*, 802, 89
- Burlon, D., Ajello, M., Greiner, J., et al. 2011, *ApJ*, 728, 58
- Brightman, M., & Nandra, K. 2012, *MNRAS*, 422, 1166
- Brunner, H., Cappelluti, N., Hasinger, G., et al. 2008, *A&A*, 479, 283
- Brusa, M., Zamorani, G., Comastri, A., et al. 2007, *ApJS*, 172, 353
- Brusa, M., Comastri, A., Gilli, R., et al. 2009, *ApJ*, 693, 8
- Brusa, M., Civano, F., Comastri, A., et al. 2010, *ApJ*, 716, 348
- Caccianiga, A., Severgnini, P., Della Ceca, R., et al. 2008, *A&A*, 477, 735
- Cappelluti, N., Brusa, M., Hasinger, G., et al. 2009, *A&A*, 497, 635
- Capak, P., Aussel, H., Ajiki, M., et al. 2007, *ApJS*, 172, 99
- Civano, F., Brusa, M., Comastri, A., et al. 2011, *ApJ*, 741, 91
- Coil, A. L., Georgakakis, A., Newman, J. A., et al. 2009, *ApJ*, 701, 1484
- Cooper, M. C., Griffith, R. L., Newman, J. A., et al. 2012, *MNRAS*, 419, 3018
- Della Ceca, R., Maccacaro, T., Caccianiga, A., et al. 2004, *A&A*, 428, 383
- Della Ceca, R., Caccianiga, A., Severgnini, P., et al. 2008, *A&A*, 487, 119
- Draper, A. R., & Ballantyne, D. R. 2009, *ApJ*, 707, 778
- Draper, A. R., & Ballantyne, D. R. 2012, *ApJ*, 751, 72
- Ebrero, J., Carrera, F. J., Page, M. J., et al. 2009, *A&A*, 493, 55
- Elvis, M., Civano, F., Vignali, C., et al. 2009, *ApJS*, 184, 158
- Enoki, M., Ishiyama, T., Kobayashi, M. A. R., & Nagashima, M. 2014, *ApJ*, 794, 69
- Georgakakis, A., Aird, J., Buchner, J., et al. 2015, *MNRAS*, 453, 1946
- Fanidakis, N., Baugh, C. M., Benson, A. J., et al. 2011, *MNRAS*, 410, 53
- Feroz, F., & Hobson, M. P. 2008, *MNRAS*, 384, L449
- Feroz, F., Hobson, M. P., & Bridges, M. 2009, *MNRAS*, 398, 1601
- Feroz, F., Hobson, M. P., Cameron, E., & Pettitt, A. N. 2013, ArXiv e-prints [arXiv:1306.2144]
- Fotopoulou, S., Salvato, M., Hasinger, G., et al. 2012, *ApJS*, 198, 1
- Frayser, D. T., Sanders, D. B., Surace, J. A., et al. 2009, *AJ*, 138, 1261
- Georgakakis, A., Carrera, F., Lanzuisi, G., et al. 2013, ArXiv e-prints [arXiv:1306.2328]
- Gilli, R., Comastri, A., & Hasinger, G. 2007, *A&A*, 463, 79
- Haardt, F., & Maraschi, L. 1993, *ApJ*, 413, 507
- Han, Y., Dai, B., Wang, B., Zhang, F., & Han, Z. 2012, *MNRAS*, 2909
- Hasinger, G. 2008, *A&A*, 490, 905
- Hasinger, G., Miyaji, T., & Schmidt, M. 2005, *A&A*, 441, 417
- Hiroi, K., Ueda, Y., Isobe, N., et al. 2011, *PASJ*, 63, 677
- Hirschmann, M., Somerville, R. S., Naab, T., & Burkert, A. 2012, *MNRAS*, 426, 237
- Hirschmann, M., Dolag, K., Saro, A., et al. 2014, *MNRAS*, 442, 2304
- Hopkins, P. F., Hernquist, L., Cox, T. J., et al. 2005a, *ApJ*, 630, 716
- Hopkins, P. F., Hernquist, L., Cox, T. J., et al. 2005b, *ApJ*, 632, 81
- Hopkins, P. F., Hernquist, L., Cox, T. J., et al. 2006, *ApJ*, 639, 700
- Hopkins, P. F., Bundy, K., Hernquist, L., & Ellis, R. S. 2007, *ApJ*, 659, 976
- Hsu, L.-T., Salvato, M., Nandra, K., et al. 2014, *ApJ*, 796, 60
- Ilbert, O., Capak, P., Salvato, M., et al. 2009, *ApJ*, 690, 1236
- Jones, L. R., McHardy, I. M., Merrifield, M. R., et al. 1997, *MNRAS*, 285, 547
- Kalfountzou, E., Civano, F., Elvis, M., Trichas, M., & Green, P. 2014, *MNRAS*, 445, 1430
- Kelly, B. C., Fan, X., & Vestergaard, M. 2008, *ApJ*, 682, 874
- Kolodzig, A., Gilfanov, M., Sunyaev, R., Sazonov, S., & Brusa, M. 2013, *A&A*, 558, A89
- Kullback, S., Leibler, R. A. 1951, *Ann. Math. Statist.*, 22, 79
- La Franca, F., Fiore, F., Vignali, C., et al. 2002, *ApJ*, 570, 100
- La Franca, F., Fiore, F., Comastri, A., et al. 2005, *ApJ*, 635, 864
- Laird, E. S., Nandra, K., Georgakakis, A., et al. 2009, *ApJS*, 180, 102
- Lilly, S. J., Le Fèvre, O., Renzini, A., et al. 2007, *ApJS*, 172, 70
- Lilly, S. J., Le Brun, V., Maier, C., et al. 2009, *ApJS*, 184, 218
- Lumb, D. H., Guainazzi, M., & Gondoin, P. 2001, *A&A*, 376, 387
- Maccacaro, T., Gioia, I. M., Avni, Y., et al. 1983, *ApJ*, 266, L73
- Maccacaro, T., Gioia, I. M., & Stocke, J. T. 1984, *ApJ*, 283, 486
- Mahmood, A., Devriendt, J. E. G., & Silk, J. 2005, *MNRAS*, 359, 1363
- Marshall, H. L., Tananbaum, H., Avni, Y., & Zamorani, G. 1983, *ApJ*, 269, 35
- Marulli, F., Bonoli, S., Branchini, E., Moscardini, L., & Springel, V. 2008, *MNRAS*, 385, 1846
- Mateos, S., Barcons, X., Carrera, F. J., et al. 2005, *A&A*, 444, 79
- Merloni, A., Predehl, P., Becker, W., et al. 2012, ArXiv e-prints [arXiv:1209.3114]
- McCracken, H. J., Capak, P., Salvato, M., et al. 2010, *ApJ*, 708, 202
- Mihara, T., Nakajima, M., Sugizaki, M., et al. 2011, *PASJ*, 63, 623
- Miyaji, T., Hasinger, G., & Schmidt, M. 2000, *A&A*, 353, 25
- Miyaji, T., Hasinger, G., Salvato, M., et al. 2015, *ApJ*, 804, 104
- Nandra, K., & Pounds, K. A. 1994, *MNRAS*, 268, 405
- Nandra, K., Laird, E. S., Aird, J. A., et al. 2015, *ApJS*, 220, 10
- Newman, J., Licquia, T., Mostek, N., et al. 2012, AAS Meeting Abstracts, #219, 219, #335.03
- Page, M. J., & Carrera, F. J. 2000, *MNRAS*, 311, 433
- Page, M. J., Carrera, F. J., Hasinger, G., et al. 1996, *MNRAS*, 281, 579
- Page, K. L., Reeves, J. N., O’Brien, P. T., & Turner, M. J. L. 2005, *MNRAS*, 364, 195
- Paltani, S., Walter, R., McHardy, I. M., et al. 2008, *A&A*, 485, 707

- Piconcelli, E., Jimenez-Bailón, E., Guainazzi, M., et al. 2005, [A&A](#), **432**, 15
- Ranalli, P., Comastri, A., Vignali, C., et al. 2013, [A&A](#), **555**, A42
- Reeves, J. N., & Turner, M. J. L. 2000, [MNRAS](#), **316**, 234
- Rovilos, E., Fotopoulou, S., Salvato, M., et al. 2011, [A&A](#), **529**, A135
- Sanders, D. B., Salvato, M., Aussel, H., et al. 2007, [ApJS](#), **172**, 86
- Salvato, M., Hasinger, G., Ilbert, O., et al. 2009, [ApJ](#), **690**, 1250
- Salvato, M., Ilbert, O., Hasinger, G., et al. 2011, [ApJ](#), **742**, 61
- Sazonov, S., Revnivtsev, M., Krivonos, R., Churazov, E., & Sunyaev, R. 2007, [A&A](#), **462**, 57
- Schmidt, M. 1968, [ApJ](#), **151**, 393
- Schmidt, M., & Green, R. F. 1983, [ApJ](#), **269**, 352
- Schwarz, G. 1978, [Ann. Stats.](#), **6**, 461
- Silverman, J. D., Green, P. J., Barkhouse, W. A., et al. 2008, [ApJ](#), **679**, 118
- Skilling J., 2004, in AIP Conf. Ser. 735, eds. R. Fischer, R. Preuss, & U. V. Toussaint, 395
- Sugizaki, M., Mihara, T., Serino, M., et al. 2011, [PASJ](#), **63**, 635
- Tomida, H., Tsunemi, H., Kimura, M., et al. 2011, [PASJ](#), **63**, 397
- Tsujimoto, M., Guainazzi, M., Plucinsky, P. P., et al. 2011, [A&A](#), **525**, A25
- Treister, E., Urry, C. M., & Virani, S. 2009, [ApJ](#), **696**, 110
- Trump, J. R., Impey, C. D., Elvis, M., et al. 2009, [ApJ](#), **696**, 1195
- Tsunemi, H., Tomida, H., Katayama, H., et al. 2010, [PASJ](#), **62**, 1371
- Ueda, Y., Akiyama, M., Ohta, K., & Miyaji, T. 2003, [ApJ](#), **598**, 886
- Ueda, Y., Hiroi, K., Isobe, N., et al. 2011, [PASJ](#), **63**, 937
- Ueda, Y., Akiyama, M., Hasinger, et al. 2014, [ApJ](#), **786**, 104
- Urry, C. M., & Padovani, P. 1995, [PASP](#), **107**, 803
- Xue, Y. Q., Luo, B., Brandt, W. N., et al. 2011, [ApJS](#), **195**, 10
- Yenko, B., Barger, A. J., Trouille, L., & Winter, L. M. 2009, [ApJ](#), **698**, 380
- Vito, F., Gilli, R., Vignali, C., et al. 2014, [MNRAS](#), **445**, 3557
- Zamojski, M. A., Schiminovich, D., Rich, R. M., et al. 2007, [ApJS](#), **172**, 468
- Zheng, X. Z., Bell, E. F., Somerville, R. S., et al. 2009, [ApJ](#), **707**, 1566